J|A|C|S ARTICLES

Published on Web 10/21/2010

Half-Sandwich Iridium Complexes for Homogeneous Water-Oxidation Catalysis

James D. Blakemore,[†] Nathan D. Schley,[†] David Balcells,[‡,§] Jonathan F. Hull,[†] Gerard W. Olack,[#] Christopher D. Incarvito,[†] Odile Eisenstein,*[,§] Gary W. Brudvig,*[,†] and Robert H. Crabtree*[,†]

Department of Chemistry, Yale University, P.O. Box 208107, New Haven, Connecticut 06520, United States, Departament de Química, Universitat Autònoma de Barcelona, 08193 Bellaterra, Barcelona, Catalonia, Spain, Institut Charles Gerhardt, Université Montpellier 2, CNRS 5253, cc 15001, Place Eugène Bataillon 34095, Montpellier, France, and Department of Geology and Geophysics, Yale University, P.O. Box 208109, New Haven, Connecticut 06520, United States

Received June 1, 2010; E-mail: robert.crabtree@yale.edu; gary.brudvig@yale.edu; odile.eisenstein@univ-montp2.fr

Abstract: Iridium half-sandwich complexes of the types Cp*Ir(N−C)X, [Cp*Ir(N−N)X]X, and [CpIr(N−N)X]X are catalyst precursors for the homogeneous oxidation of water to dioxygen. Kinetic studies with cerium(IV) ammonium nitrate as primary oxidant show that oxygen evolution is rapid and continues over many hours. In addition, $[Cp^*Ir(H_2O)_3]SO_4$ and $[(Cp^*Ir)_2(\mu\text{-}OH)_3]OH$ can show even higher turnover frequencies (up to 20 min^{-1} at pH 0.89). Aqueous electrochemical studies on the cationic complexes having chelate ligands show catalytic oxidation at pH > 7; conversely, at low pH, there are no oxidation waves up to 1.5 V vs NHE for the complexes. $H_2{}^{18}O$ isotope incorporation studies demonstrate that water is the source of oxygen atoms during cerium(IV)-driven catalysis. DFT calculations and kinetic experiments, including kinetic-isotope-effect studies, suggest a mechanism for homogeneous iridium-catalyzed water oxidation and contribute to the determination of the rate-determining step. The kinetic experiments also help distinguish the active homogeneous catalyst from heterogeneous nanoparticulate iridium dioxide.

Introduction

The oxidation of water to dioxygen is carried out by green plants, algae, and cyanobacteria in order to obtain the reducing equivalents required for sustaining life processes. Consequently, the mechanism of water oxidation has attracted considerable attention.[1] The oxygen-evolving complex (OEC), a Mn_4Ca oxo-bridged cluster in the enzyme photosystem II, catalyzes water oxidation.[2] This catalysis is thought to involve formation of a high-valent manganese oxo species, which undergoes nucleophilic attack by water, forming an O−O bond.[3] A schematic version of the proposed pathway is given in eq 1.

$$[M{=}O]^{n+} + OH_2 \rightarrow M^{(n-2)+} + O_2 + 2H^+ + 2e^- \quad (1)$$

Beyond the OEC, other synthetic catalysts are known for water oxidation.[4] Manganese model systems for the oxygen-evolving complex have been described and are most effectively driven by two-electron oxo-donating primary oxidants such as Oxone (potassium peroxymonosulfate).[5] In contrast, ruthenium water oxidation catalysts[6] have been shown to operate with one-electron primary oxidants such as cerium(IV) ammonium nitrate.[7] These one-electron oxidants may better mimic the multiple, sequential, single-electron transfer events which occur in natural photosynthesis, and studies on water-oxidation catalysts driven by these one-electron oxidants show promise for adaptation to light-driven systems (i.e., artificial photosynthesis). However, improving our understanding of water-oxidation catalysis is a key hurdle to realizing these alternative energy schemes.[8]

In 2008, Bernhard and co-workers reported the first mononuclear iridium water oxidation catalyst.[9] By treating a chloride-bridged iridium(III) dimer containing cyclometalated phenylpyridine ligands with silver triflate, they were able to generate

[†] Department of Chemistry, Yale University.
[‡] Universitat Autònoma de Barcelona.
[§] Institut Charles Gerhardt.
[#] Department of Geology and Geophysics, Yale University.

(1) (a) McEvoy, J. P.; Brudvig, G. W. *Chem. Rev.* **2006**, *106*, 4455–4483. (b) Dau, H.; Limberg, C.; Reier, T.; Risch, M.; Roggan, S.; Strasser, P. *ChemCatChem* **2010**, *2*, 724–761.
(2) Ferreira, K. N.; Iverson, T. M.; Maghloaoui, K.; Barber, J.; Iwata, S. *Science* **2001**, *303*, 1831–1838.
(3) (a) Brudvig, G. W.; Crabtree, R. H. *Proc. Natl. Acad. Sci. U.S.A.* **1986**, *83*, 4586–4588. (b) Brudvig, G. W. *Phil. Trans. R. Soc. B* **2008**, *363*, 1211–1219. (c) Brudvig, G. W.; Thorp, H. H.; Crabtree, R. H. *Acc. Chem. Res.* **1991**, *24*, 311–316.
(4) Cady, C. W.; Crabtree, R. H.; Brudvig, G. W. *Coord. Chem. Rev.* **2008**, *252*, 444–455.
(5) (a) Limburg, J.; Vrettos, J. S.; Liable-Sands, L. M.; Rheingold, A. L.; Crabtree, R. H.; Brudvig, G. W. *Science* **1999**, *283*, 1524–1527. (b) Limburg, J.; Vrettos, J. S.; Chen., H.; de Paula, J. C.; Crabtree, R. H.; Brudvig, G. W. *J. Am. Chem. Soc.* **2001**, *123*, 423–430. (c) Tagore, R.; Crabtree, R. H.; Brudvig, G. W. *Inorg. Chem.* **2008**, *47*, 1815–1823. (d) Kurz, P.; Berggren, G.; Anderlund, M. F.; Styring, S. *Dalton Trans.* **2007**, 4258–4261.

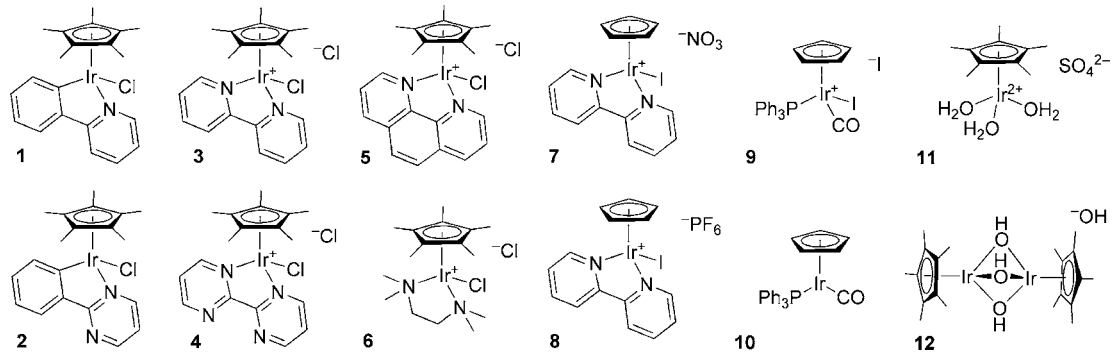

Figure 1. Iridium(III) catalysts for homogeneous water oxidation.

cationic bis-solvento iridium(III) catalyst precursors that oxidize water to dioxygen in the presence of cerium(IV) ammonium nitrate.

Since numerous iridium catalysts were available to us from work in other areas, we decided to test a selection for water-oxidizing chemistry. We focused on a catalyst precursor containing the pentamethylcyclopentadienyl ligand (Cp*), which we hoped would provide an electron rich environment, likely to stabilize the necessary high-valent intermediates required for water oxidation. In a preliminary communication, we reported Cp*Ir complexes **1** and **2** (Figure 1) as highly active catalyst precursors for water oxidation.[10] These Cp*Ir(N−C)X catalysts have turnover frequencies far above those reported for many other systems, on the order of ten turnovers per minute. Furthermore, the catalysts are mononuclear, are easy to make, and continue to catalyze oxygen evolution over hours.

We now report full details on **1** and **2** and also compare their behavior with related complexes **3**−**12** (Figure 1). In particular, the tris-aqua complex **11** and the dimer **12** can show a greater rate of oxygen evolution than that of **1**−**10** but do not follow clear first-order kinetics. In contrast, the chelate-bound precursors **1**, **3**, and **8** follow clear first-order kinetics over the entire range studied with cerium(IV) ammonium nitrate. Furthermore, moving to N−N chelate ligands yields cationic complexes **3**−**6** that are fully soluble in water, even in the iridium(III) state. This makes these systems more amenable to detailed kinetic analysis and aqueous electrochemical studies.

The presence of potentially oxidizable methyl groups on the Cp* ligand encouraged us to examine the behavior of the corresponding cyclopentadienyl (Cp) complexes. We now report synthesis and characterization of Cp complexes **7** and **8**, which have both Cp and bipyridine in the inner coordination sphere of iridium(III). Interestingly, these are the first iridium(III) complexes reported with both Cp and chelate ligands, due to the synthetic challenges associated with preparation of the Cp-containing precursors. These complexes are generally less active for water oxidation than their Cp* analogues and show lower activities per iridium at higher catalyst loadings, which suggests a multinuclear deactivation pathway or change in the rate-determining step. However, long time-course oxygen-evolution measurements suggest that the Cp complexes are less susceptible to deactivation.

A key concern in organometallic systems of the type presented here is the possibility of ligand oxidation and even degradation; in such a case, heterogeneous materials such as IrO_2 could be the true catalyst.[11] This potential heterogeneous−homogeneous ambiguity is a problem in which we have long been interested.[12] We carefully probed this question and find that the evidence favors a homogeneous origin for the catalysis at short time scales. In particular, k_H/k_D data based on initial rate data show distinct behavior for authentic IrO_2 versus catalyst **3**, although this difference in isotope effect cannot rigorously rule out the formation of unusual form(s) of iridium oxide from the various organometallic iridium precursors.

Water oxidation has been studied computationally for several catalytic systems, including mononuclear,[13] dinuclear[14] and polyoxometalate[15] Ru complexes and the oxygen-evolving complex of Photosystem II.[16] The reaction mechanisms proposed to date, which involve the participation of a high-valent metal oxo center, can be classified in two major categories: (1) O_2 formation by intramolecular coupling of two oxo ligands and (2) O_2 formation by intermolecular addition of H_2O to an oxo ligand.

(6) (a) Romain, S.; Vigara, L.; Llobet, A. *Acc. Chem. Rev.* **2009**, *42*, 1944–1953. (b) Concepcion, J. J.; Jurss, J. W.; Brennaman, M. K.; Hoertz, P. G.; Patrocinio, A. O. T.; Iha, N. Y. M.; Templeton, J. L.; Meyer, T. J. *Acc. Chem. Rev.* **2009**, *42*, 1954–1965. (c) Romero, I.; Rodríguez, M.; Sens, C.; Mola, J.; Kollipara, M. R.; Francàs, L.; Mas-Marza, E.; Escriche, L.; Llobet, A. *Inorg. Chem.* **2008**, *47*, 1824–1834. (d) Sens, C.; Romero, I.; Rodriguez, M.; Llobet, A.; Parella, P.; Benet-Buchholz, J. *J. Am. Chem. Soc.* **2004**, *126*, 7798–7799. (e) Gilbert, J. A.; Eggleston, D. S.; Murphy, W. R.; Geselowitz, D. A.; Gersten, S. W.; Hodgson, D. J.; Meyer, T. J. *J. Am. Chem. Soc.* **1985**, *107*, 3855–3864. (f) Concepcion, J. J.; Jurss, J. W.; Templeton, J. L.; Meyer, T. J. *J. Am. Chem. Soc.* **2008**, *130*, 16462–16463. (g) Concepcion, J. J.; Jurss, J. W.; Templeton, J. L.; Meyer, T. J. *Proc. Natl. Acad. Sci. U.S.A.* **2008**, *105*, 17632–17635. (h) Sala, X.; Romero, I.; Rodriguez, M.; Escriche, L.; Llobet, A. *Angew. Chem., Int. Ed.* **2009**, *48*, 2842–2852. (i) Wasylenko, D. J.; Ganesamoorthy, C.; Koivisto, B. D.; Henderson, M. A.; Berlinguette, C. P. *Inorg. Chem.* **2010**, *49*, 2202–2209. (j) Duan, L. L.; Fischer, A.; Xu, Y. H.; Sun, L. C. *J. Am. Chem. Soc.* **2009**, *131*, 10397–10398. (k) Hurst, J. K.; Cape, J. L.; Clark, A. E.; Das, S.; Qin, C. Y. *Inorg. Chem.* **2008**, *47*, 1753–1764. (l) Concepcion, J. C.; Jurss, J. W.; Norris, M. R.; Chen, Z.; Templeton, J. L.; Meyer, T. J. *Inorg. Chem.* **2010**, *49*, 1277–1279.
(7) Sridharan, V.; Menéndez, J. C. *Chem. Rev.* **2010**, *110*, 3805–3849.
(8) (a) Youngblood, W. J.; Lee, S.-H. A.; Kobayashi, Y.; Hernandez-Pagan, E. A.; Hoertz, P. G.; Moore, T. A.; Moore, A. L.; Gust, D.; Mallouk, T. E. *J. Am. Chem. Soc.* **2009**, *131*, 926–927. (b) Gust, D.; Moore, T. A.; Moore, A. L. *Acc. Chem. Rev.* **2009**, *42*, 1890–1898. (c) Hetterscheid, D. G. H.; van der Vlugt, J. I.; de Bruin, B.; Reek, J. N. H. *Angew. Chem., Int. Ed.* **2009**, *48*, 8178–8181. (d) Hurst, J. K. *Science* **2010**, *328*, 315–316.
(9) McDaniel, N. D.; Coughlin, F. J.; Tinker, L. L.; Bernhard, S. *J. Am. Chem. Soc.* **2008**, *130*, 210–217.
(10) Hull, J. F.; Balcells, D.; Blakemore, J. D.; Incarvito, C. D.; Eisenstein, O.; Brudvig, G. W.; Crabtree, R. H. *J. Am. Chem. Soc.* **2009**, *131*, 8730–8731.
(11) (a) Harriman, A.; Thomas, J. M.; Millward, G. R. *N. J. Chem.* **1987**, *11*, 757–762. (b) Nakagawa, T.; Bjorge, N. S.; Murray, R. W. *J. Am. Chem. Soc.* **2009**, *131*, 15578–15579. (c) Nakagawa, T.; Beasley, C. A.; Murray, R. W. *J. Phys. Chem. C* **2009**, *113*, 12958–12961.
(12) Anton, D. R.; Crabtree, R. H. *Organometallics* **1983**, *2*, 855–859.

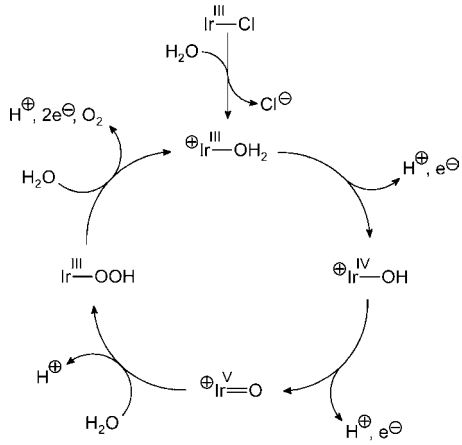

Figure 2. Reaction mechanism postulated for iridium-catalyzed water oxidation.

A plausible reaction mechanism for iridium-catalyzed water oxidation, taking into account the mononuclear nature of our catalysts, is shown in Figure 2. With a neutral chloro catalyst, such as **1** or **2**, the Cl^- ligand is replaced by a molecule of H_2O yielding a cationic Ir(III) aqua complex. This intermediate is oxidized by cerium(IV) to an Ir(V) oxo complex, which acts as active species in the formation of the O−O bond by reacting with water. The oxidation of the resulting peroxo intermediate yields the final O_2 product, and the catalyst is recovered by coordination of H_2O. In this paper, the key O−O bond formation step is characterized by means of DFT calculations.

Results and Discussion

Water Oxidation Catalyzed by 1−12. Complexes **3**−**12** were synthesized and characterized (see Experimental Section and Supporting Information), and no unusual features were encountered. In relation to our previously reported catalysts **1** and **2**,[10] **3**−**6** replace the LX-type cyclometalated ligands with the L_2-type bipyridine, phenanthroline, 2,2′-bipyrimidine, and tetramethylethylenediamine (tmeda) ligands. These compounds were isolated as their water-soluble chloride salts, having both one inner- and one outer-sphere chloride. The crystal structures of the new compounds **6** and **7** (Figure 3) confirm the expected atom connectivity.

All the complexes in Figure 1 catalyze water oxidation with cerium(IV) as primary oxidant. The initial, maximal rate of oxygen evolution is affected by changes in coordination environment; Table 1 shows the catalytic rates for **1**−**12** and some simple precursor materials. The rate of oxygen evolution is greater for **3** than for any of the analogous complexes **4**−**6**. Specifically, the tmeda complex **6** shows a slower rate than the bipyridine complex **3**. Kinetic studies suggest that tmeda is quickly protonated and lost from the iridium center under the catalytic conditions, giving essentially the same precursor as the tris-aqua complex **11**. Both **6** and **11** show a non-first-order rate dependence on catalyst concentration (vide infra), and at 5 μM catalyst, the rates of oxygen evolution from **6** and **11** are nearly identical (see Supporting Information).

The presence of potentially oxidizable, benzylic C−H bonds on the Cp* ligand could provide a site for ligand modification under the catalytic conditions. Oxidation of the Cp* ligand of $[Cp^*IrCl]_2$ has been observed upon treatment with iodine(III) reagents to give acetoxylated or hydroxylated products, depending on the reaction conditions.[17] To investigate whether a similar ligand oxidation was taking place and was involved in either catalyst decomposition or catalyst modification, we replaced the Cp* ligand with Cp. In addition to removing the oxidizable methyl groups, this change also affects the steric effect and donor power of the ligand[18] and exchange rates of the ancillary ligands.[19]

In contrast to the wealth of literature on Cp* iridium complexes, Cp complexes of iridium are much less common. This difference can be ascribed to the lack of an easily accessible and versatile starting material for their synthesis comparable to $[Cp^*IrCl_2]_2$, a readily prepared, air-stable material. The analogous CpIr dihalide materials are polymeric and not directly accessible from hydrated iridium trichloride. Instead, for the synthesis of **7** and **8** (Figure 4), we employed a procedure developed by Heinekey and co-workers[20] involving direct oxidation of $CpIr(C_2H_4)_2$ with I_2 to give $[CpIrI_2]_x$. Employing $CpIr(C_2H_4)_2$ instead of the more easily prepared $CpIr(\eta^2$-cyclooctene$)_2$ allowed us to obtain exceptionally pure material by sublimation of the bis-ethylene complex.

Looking at the Cp catalysts, we find that **7**, the analogue of Cp* complex **3**, has a slower initial turnover rate. The rates of oxygen evolution from nitrate **7** and hexafluorophosphate **8**, show essentially similar rates of oxygen evolution.[21] The nitrate salt **7** has excellent solubility in water, and this complex was

(13) (a) Kohl, S. W.; Weiner, L.; Schwartsburd, L.; Konstantinovski, L.; Shimon, L. J. W.; Ben-David, Y.; Iron, M. A.; Milstein, D. *Science* **2009**, *324*, 74–77. (b) Li, J.; Shiota, Y.; Yoshizawa, K. *J. Am. Chem. Soc.* **2009**, *131*, 13584–13585. (c) Yang, X.; Hall, M. B. *J. Am. Chem. Soc.* **2010**, *132*, 120–130. (d) Chen, Z. F.; Concepcion, J. J.; Hu, X. Q.; Yang, W. T.; Hoertz, P. G.; Meyer, T. J. *Proc. Natl. Acad. Sci. U.S.A.* **2010**, *107*, 7225–7229. (e) Wang, L.-P.; Wu, Q.; Voorhis, T. V. *Inorg. Chem.* **2010**, *49*, 4543–4553.

(14) (a) Bartolotti, L. J.; Pedersen, L. G.; Meyer, T. J. *Int. J. Quantum Chem.* **2001**, *83*, 143–149. (b) Yang, X.; Baik, M.-H. *J. Am. Chem. Soc.* **2004**, *126*, 13222–13223. (c) Yang, X.; Baik, M.-H. *J. Am. Chem. Soc.* **2006**, *128*, 7476–7485. (d) Yang, X.; Baik, M.-H. *J. Am. Chem. Soc.* **2008**, *130*, 16231–16240. (e) Romain, S.; Bozoglian, F.; Sala, X.; Llobet, A. *J. Am. Chem. Soc.* **2009**, *131*, 2768–2769. (f) Bozoglian, F.; Romain, S.; Ertem, M. Z.; Todorova, T. K.; Sens, C.; Mola, J.; Rodriguez, M.; Romero, I.; Benet-Buchholz, J.; Fontrodona, X.; Cramer, C. J.; Gagliardi, L.; Llobet, A. *J. Am. Chem. Soc.* **2009**, *131*, 15176–15187. (g) Batista, E. R.; Martin, R. L. *J. Am. Chem. Soc.* **2007**, *129*, 7224–7225. (h) Concepcion, J. J.; Tsai, M.-K.; Muckerman, J. T.; Meyer, T. J. *J. Am. Chem. Soc.* **2010**, *132*, 1545–1557.

(15) (a) Kuznetsov, A. E.; Geletii, Y. V.; Hill, C. L.; Morokuma, K.; Musaev, D. G. *J. Am. Chem. Soc.* **2009**, *131*, 6844–6854. (b) Geletii, Y. V.; Huang, Z.; Hou, Y.; Musaev, D. G.; Lian, T.; Hill, C. L. *J. Am. Chem. Soc.* **2009**, *131*, 7522–7523. (c) Geletii, Y. V.; Besson, C.; Hou, Y.; Yin, Q.; Musaev, D. G.; Quiñonero, D.; Cao, R.; Hardcastle, K. I.; Proust, A.; Kögerler, P.; Hill, C. L. *J. Am. Chem. Soc.* **2009**, *131*, 17360–17370. (d) Geletii, Y. V.; Botar, B.; Kögerler, P.; Hillesheim, D. A.; Musaev, D. G.; Hill, C. L. *Angew. Chem., Int. Ed.* **2008**, *47*, 3896–3899. (e) Sartorel, A.; Miro, P.; Salvadori, E.; Romain, S.; Carraro, M.; Scorrano, G.; Di Valentin, M.; Llobet, A.; Bo, C.; Bonchio, M. *J. Am. Chem. Soc.* **2009**, *131*, 16051–16053.

(16) (a) Lundberg, M.; Blomberg, M. R. A.; Siegbahn, P. E. M. *Inorg. Chem.* **2004**, *43*, 264–274. (b) Siegbahn, P. E. M. *Inorg. Chem.* **2008**, *47*, 1779–1786. (c) Siegbahn, P. E. M. *Acc. Chem. Res.* **2009**, *42*, 1871–1880. (d) Siegbahn, P. E. M. *J. Am. Chem. Soc.* **2009**, *131*, 18238–18239. (e) Sproviero, E. M.; Gascón, J. A.; McEvoy, J. P.; Brudvig, G. W.; Batista, V. S. *J. Am. Chem. Soc.* **2008**, *130*, 6728–6730.

(17) Park-Gehrke, L. S.; Freudenthal, J.; Kaminsky, W.; DiPasquale, A. G.; Mayer, J. M. *Dalton Trans.* **2009**, 1972–1983.

(18) Fendrick, C. M.; Schertz, L. D.; Mintz, E. A.; Marks, T. J. *Inorg. Synth.* **1992**, *29*, 193–238.

(19) (a) Wang, D.; Angelici, R. J. *Inorg. Chem.* **1996**, *35*, 1321–1331. (b) Hughes, R. P.; Lindner, D. C.; Liable-Sands, L. M.; Rheingold, A. L. *Organometallics* **2001**, *20*, 363–366.

(20) Heinekey, D. M.; Millar, J. M.; Koetzle, T. F.; Payne, N. G.; Zilm, K. W. *J. Am. Chem. Soc.* **1990**, *112*, 909–919.

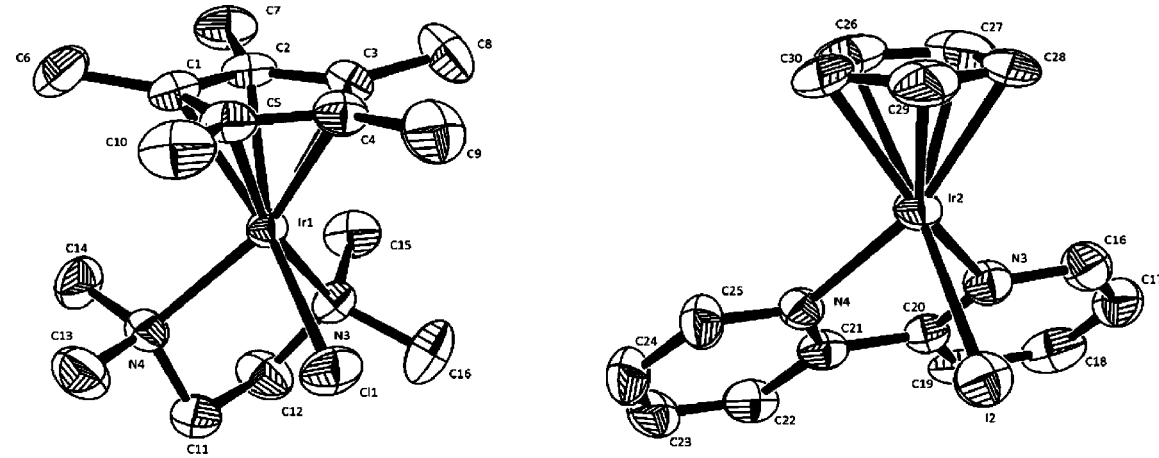

Figure 3. Crystal structures of **6** (left) and **7** (right) with ellipsoids shown at 50% probability. Counteranions have been omitted for clarity.

Table 1. Rates of Iridium-Catalyzed Oxygen Evolution

compound	formula	initial rate (μmol L^{-1} min^{-1})[a]	TOF (t.o. min^{-1})[b]
3	Cp*Ir(bipy)Cl_2	72 ± 3	14.4 ± 0.7
4[c]	Cp*Ir(bipyrim)Cl_2	19 ± 2	3.9 ± 0.4
5	Cp*Ir(phen)Cl_2	42 ± 2	8.4 ± 0.4
6	Cp*Ir(tmeda)Cl_2	31 ± 3	6.3 ± 0.6
7	[CpIr(bipy)I]NO_3	46 ± 3	9.3 ± 0.6
8[c,d]	[CpIr(bipy)I]PF_6	38 ± 2	7.6 ± 0.3
9	CpIr(PPh_3)COI_2	18 ± 1	3.5 ± 0.2
10[d]	CpIr(PPh_3)CO	17 ± 1	3.2 ± 0.1
11[c]	Cp*Ir$(H_2O)_3SO_4$	27.2 ± 0.5	5.5 ± 0.1
12[c]	[(Cp*Ir)$_2$(μ-OH)$_3$]OH	99 ± 9	10.4 ± 0.9
1[d]	Cp*Ir(ppy)Cl	49 ± 4	10.0 ± 0.9
[Cp*$IrCl_2$]$_2$[d]	[Cp*$IrCl_2$]$_2$	101 ± 5	10.1 ± 0.5
$IrCl_3 \cdot nH_2O$[c]	$IrCl_3 \cdot nH_2O$	2.1 ± 0.2	0.43 ± 0.05
K_2IrCl_6	K_2IrCl_6	0.39 ± 0.05	0.08 ± 0.01

[a] Measured by Clark-electrode oxygen assay; triplicate data sets were collected for each rate measurement. Errors (presented as $\pm 1\sigma$) were calculated from variance in the three measurements. Data were analyzed for the first 30 s of oxygen evolution. These initial rates are also the maximal rates. Conditions: 5.0($\pm$0.1) μmol L^{-1} catalyst; 78 mM Ce(IV); pH 0.89; vessel temperature maintained at 25 °C. [b] Turnovers (t.o.) are mol O_2 (mol Ir)$^{-1}$. Calculated from initial rate data. [c] Compound is isolated as a hydrate and is hygroscopic. Uncertainty in waters of hydration causes additional uncertainty in turnover numbers. [d] Catalyst injected as a solution in acetonitrile; improved analytical methods have led us to modify our previously reported rates for complex **1** and we now prefer the values given in this table; the presence of the chloride counterion was found not to accelerate the oxygen-evolution rate. The previously reported Cp*Ir(ppy)OTf analogue of **1** gives an identical rate to **1**: 47 ± 5 μmol L^{-1} min^{-1}.

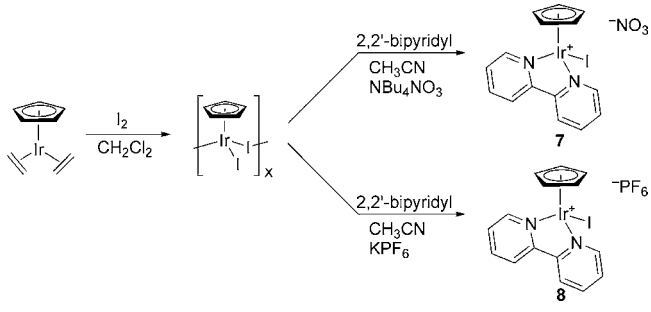

Figure 4. Synthesis of the CpIr(III) catalysts **7** and **8**.

also used for ^{18}O incorporation studies confirming incorporation of oxygen atoms from water into the product oxygen (vide infra).

In the expectation that triphenylphosphine and carbon monoxide would both be removed by irreversible oxidation, complexes **9** and **10** were studied and proved to be excellent water oxidation catalysts with similar activity to each other. These two ligands are likely lost under the catalytic conditions to yield the $CpIr(H_2O)_3^{2+}$ fragment, analogous to **11**.

To test the possibility that all the ligands on the complexes **1**−**12** were removed by oxidation, we looked at iridium trichloride. When injected into cerium(IV) solutions, $IrCl_3 \cdot nH_2O$ shows a turnover frequency of 0.4 min^{-1}, or 3% of that for **3**. Surprisingly, potassium hexachloroiridate, K_2IrCl_6, a common precursor to oxide materials of iridium[11] shows a near-zero rate of oxygen evolution. This is consistent with results obtained previously.[22]

For the bipyridine complex **3**, the initial rate of oxygen evolution is first-order in iridium (vide infra). In the first minute of catalysis with **3**, a sigmoidal response is encountered, in which a lag phase is followed by essentially constant oxygen evolution. The oxygen evolution rate reaches a maximum value within the first minute (Figure 5), in line with the behavior previously reported for catalysts **1** and **2**.[10] However, within several minutes, the rate does begin to decrease. This behavior is also seen in the case of catalyst **1** (see Supporting Information). We cannot completely exclude the possibility that the decrease in rate is the result of oxidation of the catalyst, including both the chelate ligand or the Cp* methyl groups. Since the Clark-electrode oxygen assay shows essentially no instrumental lag time, any observed lag phase is real. The lag time in Figure 5, between nominal injection of catalyst at zero time and the onset of oxygen evolution, may be a result of slow chloride dissociation from **3**, required for substrate water binding. Alternatively, since oxidation appears to be rate-limiting in these studies (vide infra), the lag phase may be related to slow oxidation of the metal complex to the required high-valent intermediate. ESI mass spectra (see Supporting Information) collected on solutions of catalyst **3** and cerium(IV) ammonium nitrate show populations of the Cp*Ir(bipy) fragment with nitrate, chloride, or hydroxide bound in the open site, suggesting an analogous solution-phase equilibrium of these species. Regardless, in the presence of a large excess of cerium(IV), the robustness of catalyst **3** seems to be limited.

(21) The salt of **8** with hexafluorophosphate counterion is hygroscopic, suggesting a source of the difference in turnover frequency when compared with **7** at the same nominal catalyst loading.

(22) Ginzburg, S. I.; Yuzko, M. I. *Russ. J. Inorg. Chem.* **1965**, *10*, 444–448.

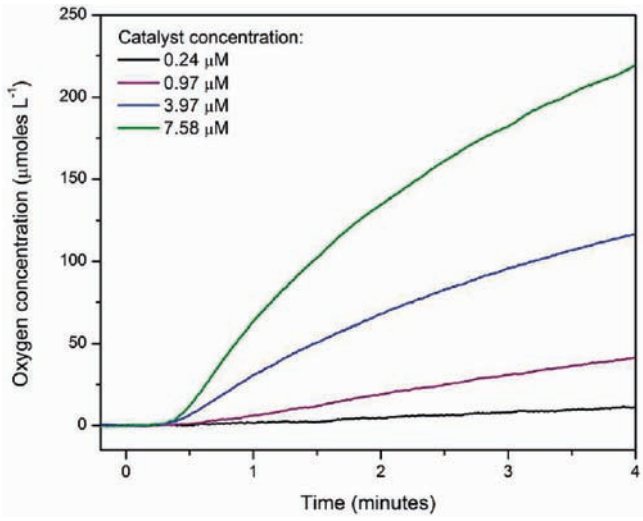

Figure 5. Oxygen-evolution traces for complex **3** as measured by Clark-electrode oxygen assay.

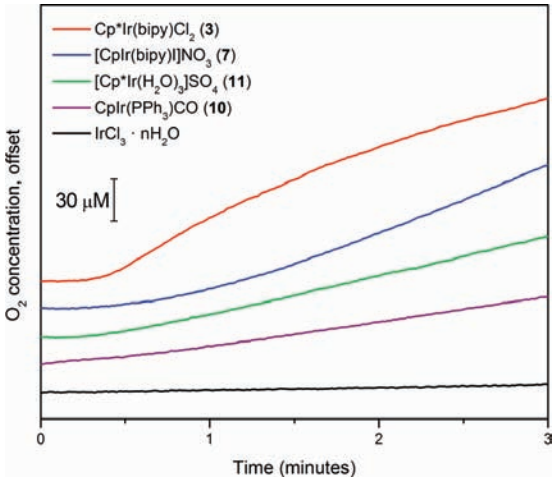

Figure 6. Comparison of oxygen evolution traces for a catalyst concentration of 5 μM.

The oxygen evolution traces differ among the various catalysts (Figure 6). Within three minutes, complex **3** has significantly dropped in rate, as noted above. The analogous Cp complex **7** shows a different trace, with no apparent deactivation up to 10 min after injection, although there is clearly lag phase-like behavior since the trace is noticeably upwardly convex. Thus, substitution of Cp* with Cp affects not only the turnover rate but also the profile of oxygen evolution and lag phase. This difference in rate profile is reflected in long timecourse studies as well (vide infra). Complexes **10** and **11** show essentially no lag phase, but **11** has a higher sustained rate of oxygen evolution. Finally, iridium trichloride hydrate shows insignificant oxygen evolution compared to the organometallic complexes. The variation in the nature of the lag phase between different complexes suggests that each complex behaves somewhat differently. For the Cp complex **7**, mass spectra show evidence of hydroxide- and nitrate-bound species in solutions with cerium(IV) ammonium nitrate. Treatment of this solution with excess ammonium hexafluorophosphate followed by extraction with dichloromethane gave [CpIr(bipy)-(*O*-NO_2)]PF_6 which we were able to crystallographically characterize (see Supporting Information). However, no iodide-bound complexes are detected in the mass spectra of **7**,

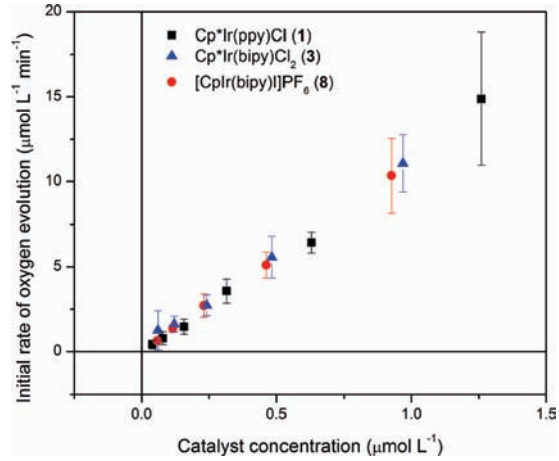

Figure 7. Dependence of oxygen-evolution rate on the concentration of catalysts **1**, **3**, and **8**.

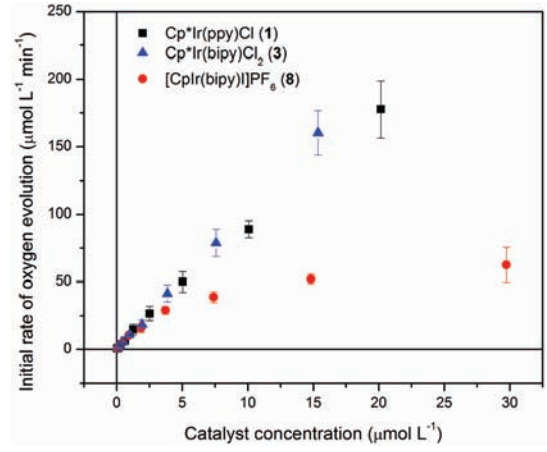

Figure 8. Dependence of oxygen-evolution rate on the concentration of catalysts **1**, **3**, and **8**.

suggesting that iodide is quickly lost from the metal center under catalytic conditions.

Although the catalysts **1**, **3**, and **8** have different rates of oxygen evolution (Table 1), a plot of the rate dependence with catalyst concentration shows that they closely resemble one another at low catalyst loadings (see Figure 7). Studies on **1** showed that oxygen evolution is first-order in iridium.[10] However, we were surprised to find that the rate of oxygen evolution for the phenylpyridine (**1**) and bipyridine (**3**) systems track each other at low catalyst loadings. Similarly, the Cp complex **8** tracks with both **1** and **3** at low catalyst loadings. A conventional log−log plot gives the order of reaction in catalyst. For **1**, **3**, and **8**, the slopes of these lines are: 0.98 ± 0.01, 0.91 ± 0.02, and 0.94 ± 0.03 (see Supporting Information for the double log plots). For each of these catalysts, the rate of oxygen evolution is essentially first-order with respect to iridium, suggesting that bimolecular steps do not contribute to catalysis with **1**, **3**, or **8**. However, at higher catalyst loadings (upward from ca. 5 μM), catalyst **8** undergoes a deactivation process and the rate of catalysis tends toward zero-order behavior (see Figure 8 and Supporting Information).

The water-oxidation behavior of complex **11**, [Cp*Ir(H_2O)$_3$]-SO_4, is surprising. Under the conditions of our Clark-electrode oxygen assay, the turnover frequency clearly increases at higher catalyst loadings. A log−log plot gives a slope of 1.31 ± 0.06, suggesting that dimerization may contribute to catalysis (see

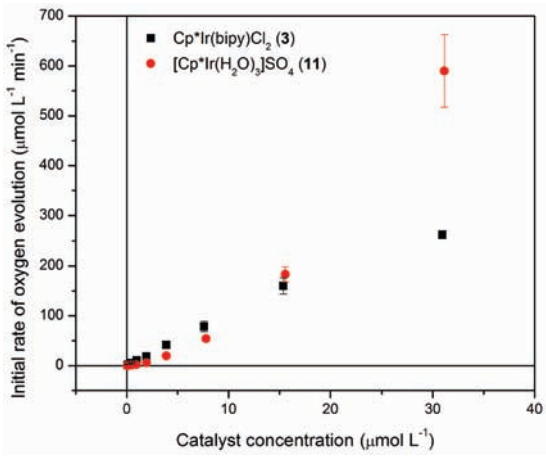

Figure 9. Dependence of oxygen-evolution rate on concentrations of **3** and **11**.

Figure 9 and Supporting Information). Additionally, the log−log plot clearly shows nonlinear behavior, suggesting equilibrium speciation processes affect the rate of oxygen evolution. For the distinct regime at higher catalyst loadings, the order in iridium is 1.64 ± 0.03. Due to the saturation of the aqueous solution with O_2 and the consequent formation of bubbles, the upper limit for the Clark assay, which only records dissolved O_2, is around 30 μM for the tris-aqua complex. Even with this limitation, at this catalyst loading, a turnover frequency of 20 min^{-1} is seen.

With the complex **11** in hand, we next moved to characterize the behavior of the related dimer **12**. On a per-iridium basis, the performance of complexes **11** and **12** is similar at 5 μM catalyst. However, at higher loadings of the dimer **12**, the rate of oxygen evolution is greater than first-order in iridium, with a log−log plot slope of 1.53 ± 0.05 (see Supporting Information), again suggesting that the dimeric structure of **12** contributes to oxygen evolution. The non-first-order behavior at low loading of catalyst suggests a monomer−dimer equilibrium that affects the rate of catalysis. Turnover frequencies for the dimer **12** are up to 25 turnovers min^{-1} on a per-iridium basis, or 50 min^{-1} on a dimer basis.

In our original report on water-oxidation catalysis with Cp*Ir complexes, we noted that $[Cp^*IrCl_2]_2$ was competent for oxygen evolution. We have confirmed this result here, and find high turnover numbers with this system. However, this dimeric material shows a similar concentration-dependent rate plot when compared to **12** (see Supporting Information). As with **12**, this suggests that a dimeric structure contributes to catalysis.

Chloride oxidation to hypchlorite or chlorine gas is a potentially competing reaction in these water-oxidizing systems. Comparing the rates of the compounds Cp*Ir(ppy)Cl (**1**) and Cp*Ir(ppy)OTf, we see no difference either in the observed initial rate of water oxidation or in the appearance of the subsequent oxygen-evolution data. Similarly, with dimers $[Cp^*IrCl_2]_2$ and **12**, there is no significant change in initial rate or catalytic behavior. This suggests that the presence of chloride does not significantly impact the water oxidation reaction in these systems. This also applies to the Cp-containing systems, since upon chloride addition to solutions of chloride-free catalyst **7**, no significant change in oxygen evolution is observed.

Solutions containing catalysts and excess oxidant continue to evolve oxygen over hours (see Table 2). For example, a solution with catalyst **3** gives a total of 320 turnovers in 8 h.

Table 2. Catalyst Turnovers Measured with Headspace Oxygen Assay[a]

compound	formula	turnovers in first hour	turnovers in 8 h	turnovers per hour
1	Cp*Ir(ppy)Cl	155	349	44
3	$Cp^*Ir(bipy)Cl_2$	93	320	40
7	$[CpIr(bipy)I]NO_3$	214	738	92
11	$[Cp^*Ir(H_2O)_3]SO_4$	128	281	35

[a] Conditions: 5.0 μmol L^{-1} catalyst; 78 mM Ce(IV); pH 0.89; vessel temperature maintained at 21 °C; turnovers are defined as mol O_2 (mol Ir)$^{-1}$. Turnovers per hour are the average over the 8-h run. Error is ±5% for the first hour, and ±9% after 8 h, reflecting increased uncertainty at long reaction times (triplicate measurements).

This gives an overall turnover frequency of 40 per hour.[23] The complexes **1** and **11** give similar initial turnover numbers and overall frequencies. On the basis of these results and the appearance of the oxygen-evolution traces (see Supporting Information), the catalysts are deactivated within the first two hours of catalysis. This is also observable in the initial rate data, as most of the Cp*-bearing compounds show decreases in rate within minutes of injection. We cannot exclude the possibility that the decrease in rate is the result of oxidation of the catalyst, such as of the chelate ligand or of the Cp* methyl groups. If the chelate ligand alone were oxidized and lost, we would expect to obtain activity like that of the tris-aqua species; this is not observed (Table 2). If the Cp* were also oxidized and/or lost, catalytically active Ir−O particulate species could be formed. The first few minutes of reaction are kinetically well-behaved and are ascribed to homogeneous catalysis, but the origin of the longer term activity cannot be so confidently ascribed. With all this in mind, it is intriguing to note that Cp complex **7** gives a much higher overall turnover number but a lower initial rate. This agrees with initial rate data collected by Clark electrode and points to increased oxidative stability of the catalyst. Indeed, compared to **1**, **3**, or **11**, Cp-catalyst **7** shows more than double the turnover frequency over 8 h.

Water was confirmed as the source of the oxygen gas produced by using measurements of ^{18}O-incorporation. Stable isotope ratio mass spectrometry (SIR-MS, see Experimental Section) is exquisitely sensitive to changes in isotopic abundance in gases, and examines parts per thousand (ppt) changes in isotope distribution of near natural-abundance systems. Consequently, only a small amount of isotope label is required. In the first experiment, purified natural-abundance H_2O was used to prepare solutions of cerium(IV) oxidant and catalyst **7**. Upon injection of catalyst, oxygen evolution commenced and reached a steady rate, giving a total $^{18}O/^{16}O$ ratio of 0.200%. In the second experiment, a small amount of 95% $H_2{}^{18}O$ in natural-abundance H_2O was used to prepare solutions of cerium(IV) and **7**,[24] with the result that the $^{18}O/^{16}O$ ratio was then 0.217%. The expected change in the $^{18}O/^{16}O$ ratio was 0.023% based on the added ^{18}O label. This is in good agreement with the measured 0.017% change, which corresponds to a change of 8.5 ppt, and confirms that water is the source of the oxygen gas produced.

Among homogeneous water-oxidizing systems, ruthenium catalysts are among the best characterized.[6,13] In this context, analogues of **3** were synthesized with ruthenium, as well as rhodium. No oxygen evolution activity was detected using

(23) There was sufficient cerium(IV) for more than 3500 turnovers.
(24) A 35 μL amount of 95% $H_2{}^{18}O$ was added to 12.5 mL of natural-abundance H_2O.

cerium(IV) as primary oxidant for Cp*RuCl(2,2′-dipyridyl), RuCl(2-phenylpyridine-$\kappa C,N$)(*p*-cymene), and [Cp*RhCl(2,2′-dipyridyl)]Cl. We anticipate that the lack of water-oxidizing behavior is due to kinetically slow oxidation of the metal complexes, which limits access to the high-valent intermediates required for oxygen evolution.

A surprising feature of the experimental work is the near independence of the results on the nature of the chelating ligand employed. We, therefore, considered the possibility that the chelating ligand was removed under the oxidizing conditions and that the true catalyst is always solvated $[Cp^*Ir]^{2+}$. Kinetic studies show that while the reaction is first-order in catalyst for compounds containing chelate ligands, **1** and **3**, the order of the reaction is greater than one for the solvated $[Cp^*Ir]^{2+}$ fragment, **11**, which suggests loss of chelating ligand is not occurring. This is consistent with ESI+ MS data, which show retention of both the Cp*/Cp and chelate ligands for catalysts **3** and **8** upon treatment with excess cerium(IV). Finally, the oxygen-evolution rates of compounds **3**, **4**, **5**, and **6** vary (above the level of experimental error) with the identity of the chelate ligand, suggesting that the choice of ligand, slightly but significantly, affects the rate of catalysis.

Comparison of our work with the prior experimental studies cited above[4−6] indicates that the present catalysts may have certain advantages. These catalysts provide good activity and are suitable for electrochemical or spectroelectrochemical studies. They have an easily modified ligand environment, a factor that may assist in their attachment to other components of more elaborate architectures, such as a solar water-splitting cell. However, the kinetic behavior of the complexes, at least with the harsh conditions required for use of cerium(IV) as primary oxidant, suggest that long-term robustness may be limited with these catalysts. Generally, though, as a third row metal, the metal−ligand bonds are also expected to be much more robust, kinetically and thermodynamically, than in the case of base metal catalysts such as our own terpyridine−Mn system[5] or than the second row systems based on Ru.[6] Building on Bernhard's work,[9] they also open up the way to the use of organometallic precursors for water-oxidation catalysis. On the other hand, iridium is a precious metal, so high value and research applications seem the most appropriate.

Aqueous Electrochemistry. Cerium(IV) studies are limited to the strongly acidic pH values needed to stabilize the oxidant. However, electrochemistry allows us to examine the oxidation behavior of these complexes over a much wider pH range. Although electrochemistry with complex **1** is possible in acetonitrile (see Supporting Information), the complex is not soluble in aqueous solutions in the iridium(III) oxidation state. The cationic iridium(III) complexes **3**−**6**, **7**, and **11** are soluble in water, allowing us to now examine electrochemically driven oxidations in aqueous solution.

Cyclic voltammograms collected for complex **3** at various pH values are shown in Figure 10. A prominent catalytic wave at ca. pH = 12, assigned to catalytic water oxidation, is associated with the complex. Below pH = 7, there is no oxidation up to 1.5 V vs NHE, suggesting that catalysis with cerium(IV) occurs at oxidizing potentials above 1.5 V. This is consistent with the literature redox potential for cerium(IV), ca. 1.61 V.[25] Additionally, the Nernst equation dictates that the oxidizing potential of a concentrated solution of cerium(IV) will be greater than this literature value, which is calculated for

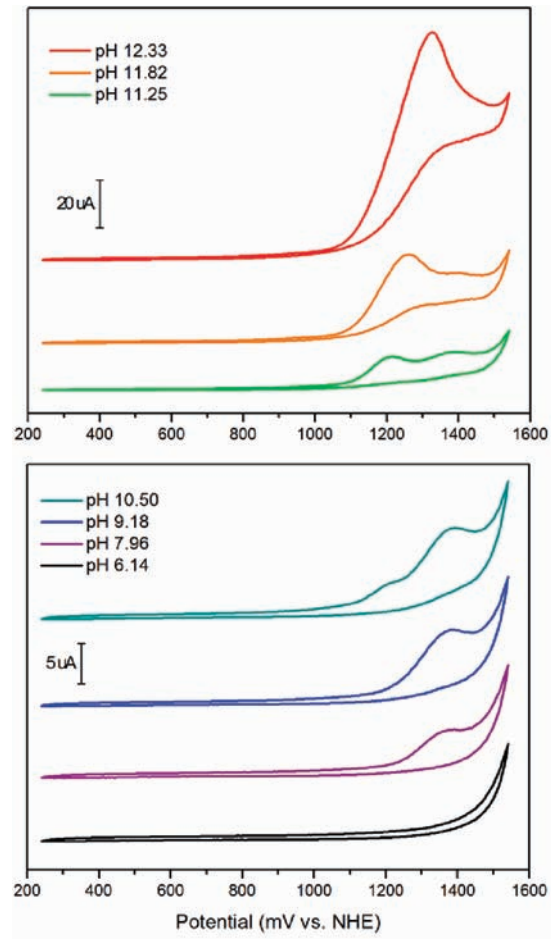

Figure 10. pH-dependent cyclic voltammograms of complex **3** in aqueous solution (scan rate: 20 mV/s; electrode surface area: 0.09 cm^2).

equimolar solutions of cerium(IV) and cerium(III). Since we prepare solutions of cerium(IV) which can be conservatively expected to initially contain less than 1% cerium(III), the oxidizing power of the cerium(IV) solutions used in the chemical oxidant-driven catalysis is as high as 1.7 V. Thus, at low pH values, the potential required for oxygen evolution is likely above 1.5 V.

In the range of pH 7−11.5, irreversible oxidation waves appear between 1.15 and 1.35 V vs NHE. At higher pH values (ca. 11), the lower potential wave at ca. 1.15 V grows in intensity, eventually becoming the dominant, catalytic oxidation at pH = 12. The current at higher pH values exceeds the current at the lower pH values, consistent with catalysis. From the appearance of the voltammograms, the catalysis is not occurring under purely kinetic conditions, as described by Savéant.[26] This may be a consequence of a fast rate of reaction compared to diffusion at the chosen scan rate of 20 mV/s. Regardless, the appearance of multiple oxidation waves suggests that different reactions take place as the pH is changed. This may be related to a pH-dependent speciation process, resulting in bound water deprotonation at higher pH values, or pH-dependent reactions of oxidized species. Such a speciation process would be expected to affect the catalytic behavior of the metal complex, as is seen in the voltammograms in Figure 10.

Alternatively, the 2 equiv of chloride present in solution could be oxidized to chlorine or hypochlorite. However, oxidative

(25) Schilt, A. A. *Anal. Chem.* **1963**, *35*, 1599–1602.

(26) Savéant, J.-M. *Chem. Rev.* **2008**, *108*, 2348–2378.

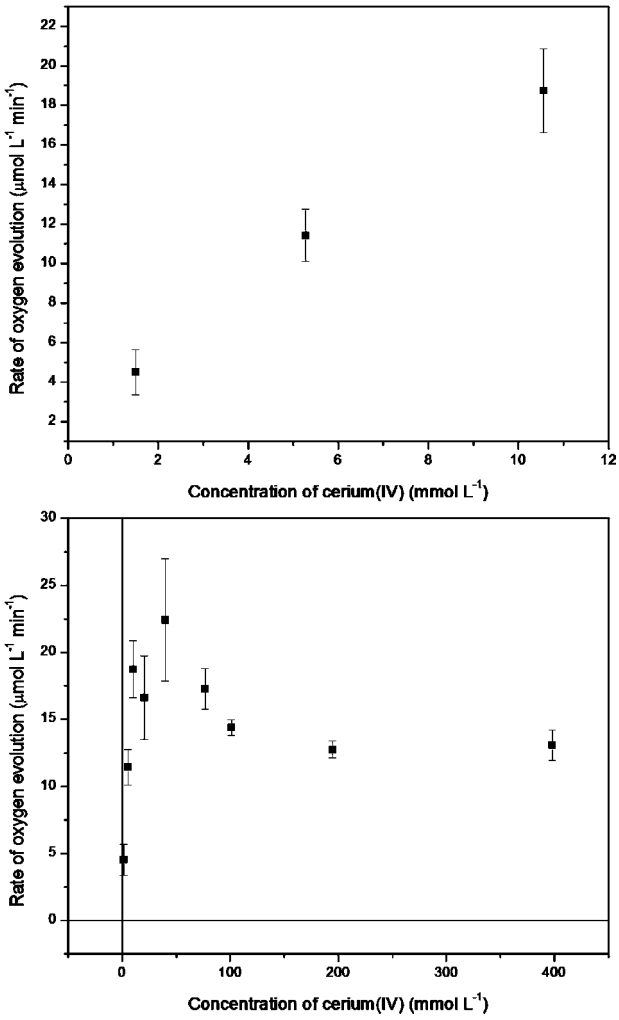

Figure 11. Oxygen-evolution rate dependence on the concentration of cerium(IV).

background scans run with equivalent concentrations of chloride without the iridium complex do not show significant currents. Furthermore, upon multiple oxidizing scans in cyclic voltammetry, the oxidation waves seen for complex **3** do not decrease in intensity. This is consistent with a catalytic process, rather than stoichiometric oxidation of chloride. Finally, since chloride oxidation is a pH-independent process, whereas water oxidation is pH dependent, the increasingly intense oxidations observed for **3** at higher pH values are consistent with water oxidation. pH dependent electrochemistry for complex **4** is very similar to that of **3** and is provided in the Supporting Information. The electrochemical behavior of **3** and **4** is reversible upon acidification. Complexes **11** and **12** show complex and unique electrochemical behavior, which is discussed elsewhere.[27]

Rate Dependence on the Concentration of Cerium(IV) and Kinetic Isotope Effects. A plot of the cerium(IV) concentration-dependence of oxygen evolution for complex **3** (Figure 11) shows two regimes. At lower cerium(IV) concentration, the kinetics are less than first-order in oxidant, with a log−log plot slope of 0.73 ± 0.01 (see Supporting Information). At higher loadings, the kinetics become zero-order in cerium(IV). This change in kinetic behavior suggests that the rate-determining step (rds) has changed. With a low oxidant loading, the rds may be the oxidation of the catalyst to a high-valent metal-oxo active species, whereas at higher oxidant loading, the rds may be the formation of the O−O bond of the final O_2 product (vide infra). For complex **11**, the rate of oxygen evolution is zero-order in oxidant (see Supporting Information).

Table 3. Summary of KIE Data

compound	KIE at 8 mM cerium(IV)	KIE at 243 mM cerium(IV)
3	0.65	1.15
IrO_2 nanoparticles	1.60	−

In order to distinguish between homogeneous and heterogeneous catalysis, we undertook a study of the H/D kinetic isotope effect by determining the k_H/k_D ratio for both our organometallic complex **3** and IrO_2 nanoparticles (Table 3) using Clark-electrode oxygen-evolution data. Since the rate-determining step appears to change based on the oxidant concentration for **3**, the kinetic isotope effect (KIE) was measured in the two distinct regimes. For complex **3**, at 8 mM cerium(IV), the measured KIE is 0.65. This is a large and relatively unusual inverse isotope effect, which corresponds to a near doubling of the rate of water oxidation when D_2O is substituted for H_2O.

This inverse KIE is consistent with rate-determining oxidation from Ir(IV) to Ir(V) occurring by way of a transition state containing a cerium(IV) bound to the iridium(IV) center via a bridging hydroxyl group. Upon formation of this transition state, the hybridization at the oxygen center will become sp^2, causing an increase in the O−H bond strength. The O−D bond will strengthen more than the O−H bond, resulting in the measured inverse KIE. Although there is no precedent for an inverse KIE in water oxidation, there is precedent for inverse isotope effects during the formation or cleavage of C−H bonds at metal centers.[28] Often these inverse isotope effects involve pre-equilibrium conditions, which give rise to the observed variation in rate. In the case of the inverse isotope effect measured for complex **3**, pre-equilibrium coordination of Ce(IV) to the hydroxyl group of Ir(IV) is consistent with the near first-order dependence on oxidant found in our experiments (vide supra).

In contrast, at 8 mM cerium(IV), iridium dioxide nanoparticles give a very different KIE of 1.6. This normal isotope effect is consistent with rate-determining O−O bond formation occurring by nucleophilic attack of water to an iridium oxo species. Furthermore, oxygen evolution rapidly decays in the case of iridium dioxide nanoparticles, already attaining a near-zero rate within 15 min from the time of injection into the cerium(IV) solution. IrO_2 has been shown previously to have poor performance for oxygen evolution with cerium(IV).[11a]

With complex **3** at 243 mM cerium(IV), the measured KIE is 1.2. This value is also consistent with rate-determining O−O bond formation. The value for this KIE is similar to other measured kinetic isotope effects observed for O−O bond formation and is best considered a secondary isotope effect. For example, *cis*,*cis*-$[(bipy)_2Ru(H_2O)]_2O^{4+}$ and $[(terpy)Mn(H_2O)O]_2^{3+}$ have been found to have KIE values for oxygen evolution of 1.7 and 1.64, respectively.[5b,29] For IrO_2 at 243 mM cerium(IV), no catalysis was observed. Upon injection of the nanoparticles into the oxidant, a short and rapid burst of oxygen release was detected, consistent with stoichiometric release of oxygen from the nanoparticles.

(27) Blakemore, J. D.; Schley, N. D.; Olack, G. W.; Incarvito, C. D.; Brudvig, G. W.; Crabtree, R. H. *Chem. Sci.* **2010**, DOI: 10.1039/c0sc00418a.
(28) (a) Janak, K. E. In *Comprehensive Organometallic Chemistry III*; Crabtree, R. H.; Mingos, M. P., Eds.; Elsevier: Oxford, 2007. (b) Parkin, G. *Acc. Chem. Res.* **2009**, *42*, 315–325.

From the above information, it is clear that the homogeneous catalyst **3** has a distinct behavior from the previously studied nanoparticulate IrO_2 material. The differences in KIE data show that oxidation to the key intermediate required for O−O bond formation occurs through different intermediates in complex **3** versus IrO_2. The rapid decay in activity at 8 mM cerium(IV) and the lack of catalytic activity at higher oxidant concentrations demonstrate that the catalyst from organometallic complex **3** is distinct from the nanoparticulate IrO_2 material, when water oxidation is driven with cerium(IV). Furthermore, examination by transmission electron microscopy (TEM) of solutions containing cerium(IV) and catalyst **3** do not show any evidence for formation of nanoparticulate (IrO_2) materials.

Mallouk et al. have previously shown that iridium dioxide nanoparticles have a KIE value of 1.0 for oxygen evolution, when oxidized with $[Ru(bipy)_3]^{3+}$.[30] The kinetic data for the nanoparticles suggested that the rate-determining step was oxidation from Ir(III) to Ir(IV). Since these results are different than those obtained here with cerium(IV), it appears that the nature of the primary oxidant used to drive water oxidation is closely tied to the kinetics of oxygen evolution. Additionally, the identity of the catalytically competent oxidation state for O−O bond formation in various iridium oxide systems has been debated. Harriman et al. have implicated an iridium(V) species as the catalytically competent intermediate required for oxygen evolution in iridium oxide colloids,[31] while Murray et al. have implicated an iridium(VI) species as the catalytically competent intermediate in electrochemically driven systems with small nanoparticles.[11b,c]

DFT Calculations on the Formation of the O−O Bond. The formation of the O−O bond is one of the key steps in the oxidation of water to dioxygen.[13,15] This step is studied at the DFT(B3LYP) level (see Computational Details) for catalyst **1** (Figure 1), which is modeled by replacing the Cp* ligand by Cp. Following the reaction mechanism represented in Figure 2, our model catalyst is oxidized to an Ir(V) oxo complex, $CpIrO(ppy)^+$, which promotes O−O bond formation by reacting with water. In view of the high catalytic activities observed in our experiments, this step should involve a low energy pathway.

The challenging O−O bond formation step requires the coupling of two O atoms having opposite reactivity, since the O of H_2O has to act as nucleophile, whereas the O of the metal-oxo has to act as electrophile. Because of the poor nucleophilic character of H_2O, a highly electrophilic metal-oxo active species is needed for efficient catalysis. The ability of $CpIrO(ppy)^+$ to promote the formation of an O−O bond with H_2O stems from its electronic structure. As noted in our previous work,[10] the set of orbitals associated with the Ir═O π bond (Figure 12) is filled with six electrons. Four of them are in the two bonding $d_\pi+p_\pi$ orbitals, π_N and π_C, whereas the other two are in the antibonding π^*_N orbital. The presence of the doubly occupied π^*_N orbital, which is preferentially located on Ir rather than on O, increases the electrophilicity of O and weakens the Ir═O bond. The electrophilicity of the oxo ligand is also promoted by the presence of the empty π^*_C orbital, which lies low in energy at the LUMO level.

The proposed active species, $CpIr(O)(ppy)^+$, is mononuclear and contains only one oxo ligand. Therefore, a reasonable mechanism for O−O bond formation is the intermolecular attack

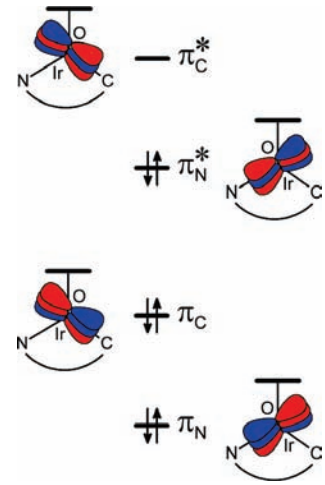

Figure 12. Schematic d_π-p_π Ir═O orbitals of $CpIr(O)(ppy)^+$ seen down the Ir═O axis.

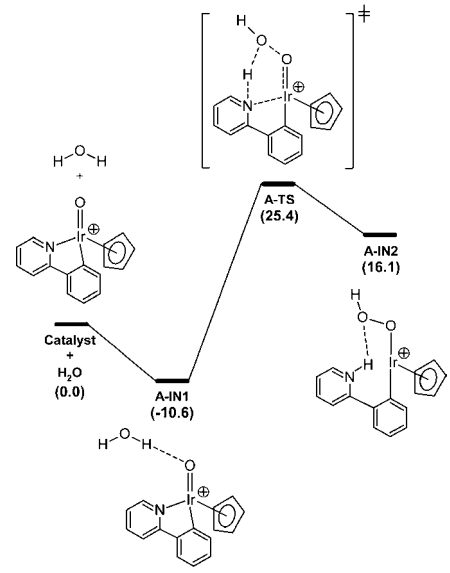

Figure 13. O−O bond formation in pathway A. Energies are given in kcal mol^{-1}.

of H_2O to the oxo ligand.[32] A key point of this pathway is that one proton has to transfer from H_2O to some proton acceptor, in order to benefit from the enhanced nucleophilicity of the incipient hydroxide ion. The nature of the proton acceptor is explored in our calculations. Three different mechanisms, labeled as **A**, **B**, and **C** (Figures 13−15), are characterized, each one involving a different proton acceptor. The global stabilizing effect of water on all extrema is evaluated by single-point calculations using the CPCM method (see Computational Details). The counterion is not explicitly introduced in the modeling since the cations and anions most likely form solvent separated ion pairs in water. Since the final product is a d^6 Ir(III) low spin complex, the calculations are carried out for the singlet electronic state.[33]

(29) Yamada, H.; Siems, W. F.; Koike, T.; Hurst, J. K. *J. Am. Chem. Soc.* **2004**, *126*, 9786–9795.
(30) Morris, N. D.; Suzuki, M.; Mallouk, T. E. *J. Phys. Chem. A* **2004**, *108*, 9115–9119.
(31) Nahor, G. S.; Hapiot, P.; Neta, P.; Harriman, A. *J. Phys. Chem.* **1991**, *95*, 616–621.
(32) Alternatively, O−O bond formation may involve OH^- instead of H_2O, because OH^- is much more nucleophilic than H_2O. Nevertheless, at the strongly acidic pH at which the reaction is performed, the hydroxide concentration is more than 10 orders of magnitude lower than that of H_2O.

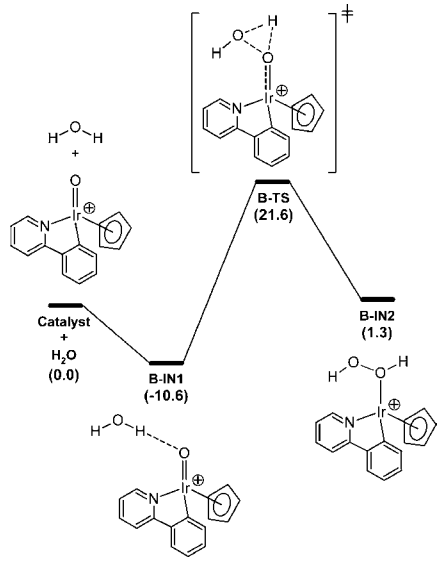

Figure 14. O−O bond formation in pathway B. Energies are given in kcal mol^{-1}.

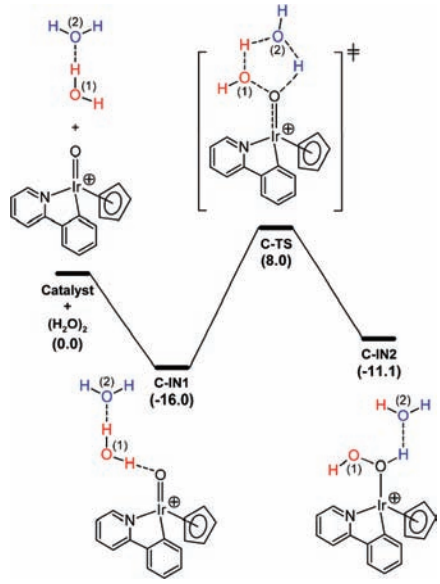

Figure 15. O−O bond formation in pathway C. Energies are given in kcal mol^{-1}.

In pathway A (Figure 13), the N of the ppy ligand acts as proton acceptor. The reaction starts with the formation of an intermediate, **A-IN1**, in which the oxo ligand is H-bonded to a molecule of H_2O, d(H···O) = 1.89 Å. This complex lies 10.6 kcal mol^{-1} below the starting reactants. In the following step, **A-IN1** is transformed into the hydroperoxo complex **A-IN2**, in which the O−O bond has been formed, d(O−OH) = 1.48 Å, and the N of the ppy ligand has been protonated, d(N−H) = 1.05 Å. The protonation of the N of ppy causes the cleavage of the Ir−N bond; 2.07 Å in **A-IN1**, 3.43 Å in **A-IN2**. In the transition state, **A-TS**, the O of H_2O approaches the oxo ligand, d(O···O) = 1.85 Å, and transfers one proton to the N of the ppy ligand, d(O···H) = 1.21 Å and d(H···N) = 1.27 Å. The three atoms involved in the proton transfer are very close to the expected linear arrangement, α(O···H···N) = 174.0°. Pathway A is endothermic by 16.1 kcal mol^{-1} and involves a transition state lying 25.4 kcal mol^{-1} above reactants. These results show that O−O bond formation is endothermic and involves a significant energy barrier when the proton of H_2O is transferred to the N of the ppy ligand.

In pathway B (Figure 14), the oxo ligand of CpIrO(ppy)$^+$ not only generates the new O−O bond, but it also accepts the proton released by H_2O, i.e., the oxo inserts into the O−H bond. In the transition state, **B-TS**, the formation of the O−O bond, d(O···O) = 1.99 Å, is concerted with the proton transfer from H_2O to oxo, d((H)O···H) = 1.53 Å and d(O···H) = 1.00 Å. The relaxation of **B-TS** toward reactant and product yields intermediates **B-IN1**, which is analogous to **A-IN1**, and **B-IN2**, respectively. In **B-IN2**, the dihydroperoxide product is formed, d(HO−OH) = 1.46 Å, and κ^1-bound to Ir, as illustrated by the two different Ir−OH distances of 2.24 Å and 3.11 Å. The energies associated with the transition state and product of pathway B, 21.6 kcal mol^{-1} and 1.3 kcal mol^{-1}, respectively, are lower than those associated with pathway A. This suggests that O−O bond formation is more favorable when the proton released by H_2O is transferred to the oxo ligand, rather than to the N of the ppy ligand.

Pathway B may be further accelerated by including an additional water molecule to assist the proton transfer. In the real system, the catalyst is solvated by H_2O, which may, therefore, act both as reactant, by promoting the formation of the O−O bond, and as cocatalyst, by assisting the water-to-oxo proton transfer. This possibility is explored by introducing one additional molecule of H_2O in the more favorable pathway, B, which is named pathway C (Figure 15). The stabilizing influence of water was also explored for pathway A but this pathway D is found to be energetically less favorable than pathway C and is not presented further (see Supporting Information for further details).[34]

In the prereaction complex, **C-IN1**, the catalyst interacts with a water dimer through a H-bond, d(H···O(Ir)) = 2.06 Å. In the cyclic transition state, **C-TS**, $H_2O(1)$ attacks the oxo ligand, whereas $H_2O(2)$ assists the proton transfer. **C-TS** involves the concerted formation and cleavage of three bonds: (1) O−O bond formation by $H_2O(1)$, d(O···O) = 1.50 Å, (2) proton transfer from $H_2O(1)$ to $H_2O(2)$, d(O···H) = 1.40 Å and d(H···O) = 1.08 Å, and (3) proton transfer from $H_2O(2)$ to the oxo ligand, d(O···H) = 1.00 Å and d(H···O) = 1.86 Å. This is a proton transfer chain in which one proton is transferred through $H_2O(2)$ and involves a planar five-membered ring (Ir═)O···O(1)···H···O(2)···H···O(═Ir), dihedral angle Ω(O···O(1)···H···O(2)) = 2.2°. The relaxation of **C-TS** toward product yields a dihydroperoxo complex, **C-IN2**, which is analogous to **B-IN2**. Pathway C is exothermic by −11.1 kcal mol^{-1} and involves a low energy transition state, which lies 8.0 kcal mol^{-1} above reactants. These results show that O−O bond formation by CpIrO(ppy)$^+$ involves a low energy pathway when the two following requirements are fulfilled: (1) the oxo ligand, rather than to the N of the ppy ligand, acts as proton acceptor and (2) the proton transfer is assisted by an additional molecule of water.

The kinetic isotope effect (KIE) has been also calculated using all frequencies. The k_H/k_D values computed for pathways A, B,

(33) The triplet state of CpIrO(ppy)$^+$, which is generated by promoting one electron to the π^*_C orbital, has radical oxyl character, with a local spin density on oxygen of 1.14. Some theoretical studies have suggested that oxyl character promotes water oxidation in photosystem II (ref 16a). Nevertheless, we find that water oxidation by CpIrO(ppy)$^+$ becomes much more endothermic in the triplet oxyl state. For example, the ΔE associated with **A-IN1** → **A-IN2** increases from 26.7 kcal mol^{-1}, in the singlet, to 52.4 kcal mol^{-1}, in the triplet. This is due to the reduction of the metal center from Ir(V) to Ir(III), which, in the octahedral environment of the catalyst, has strong preference for a low spin diamagnetic configuration.

and C are 4.1, 2.2, and 1.6, respectively.[35] The decrease of k_H/k_D from A to B and from B to C, shows that the amount of O−H cleavage in the transition state relative to reactant is smaller for the proton transfer to the oxo ligand (B) than to the N of the ppy ligand (A) and is further reduced when the proton transfer is assisted by H_2O (C). Interestingly, the A > B > C trend in k_H/k_D parallels that of the transition state energies, which suggests that O−H cleavage has a critical influence on the energy barrier. The KIE calculated for pathway C, 1.6, which is normal and secondary, is close to the experimental value obtained for **3** at high cerium(IV) concentration, 1.15 (Table 3), when O−O bond formation would be the rate-determining step. These results support pathway **C** as a plausible mechanism for the formation of the O−O bond. In the experimental conditions, the proton transfer may be further assisted by more molecules of H_2O, which would reduce even further both the calculated energy barrier and KIE.

The calculations show that the energy barrier for the formation of the O−O bond is significantly influenced by the nature of the proton acceptor. The intramolecular proton transfer to the nitrogen of the coordinated ppy ligand is less favorable than to an outer-sphere water molecule. In contrast, a theoretical study by Yang and Hall on Ru-catalyzed water oxidation, suggests that the O−H bond is cleaved intramolecularly.[13c] However, the participation of outer-sphere water has been invoked in related chemistry[13b] and is involved in water oxidation by Ru polyoxometallates.[15a] Participation of the solvent in proton transfer reactions involving transition metal complexes is well documented[36] and also seems to be of great importance in the present case.

In summary, our calculations show that the metal oxo active species, modeled by $CpIrO(ppy)^+$, is capable of forming an O−O bond by intermolecular attack of H_2O to the oxo ligand. This reaction is accompanied by a proton transfer from H_2O to the oxo ligand, which is assisted by an additional molecule of H_2O.

Conclusions

Iridium half-sandwich complexes Cp*Ir(N−C)X, [Cp*Ir(N−N)X]X, and [CpIr(N−N)X]X are highly active catalyst precursors for the homogeneous oxidation of water to dioxygen. Kinetic studies with cerium(IV) ammonium nitrate as primary oxidant show that oxygen evolution is rapid and continues over many hours. In addition, $[Cp^*Ir(H_2O)_3]SO_4$ and $[(Cp^*Ir)_2(\mu\text{-}OH)_3]OH$ show even higher turnover frequencies. Aqueous electrochemical studies on the water-soluble cationic complexes show a catalytic oxidation wave at a potential of 1.2−1.4 V at pH > 7.0 but, at lower pH, show no oxidation waves below 1.5 V vs NHE. $H_2{}^{18}O$ isotope incorporation studies show that water is the source of oxygen atoms during cerium(IV)-driven catalysis. DFT calculations show that in the key O−O bond formation step, water attacks the oxo ligand of the active species by losing one proton. The energy profile associated with this reaction is significantly lowered when the proton is transferred to the oxo ligand with the assistance of one additional molecule of water.

Experimental Section

General. All solvents were of commercial grade and dried over activated alumina prior to use. Chloride-free tetra-*n*-butylammonium nitrate was prepared by shaking an aqueous solution of sodium nitrate and tetrabutylammonium hydrogen sulfate in a separatory funnel and extracting the product with dichloromethane.[37] All other reagents were obtained from major commercial suppliers and used without further purification. $[Cp^*IrCl_2]_2$,[38] $CpIr(C_2H_4)_2$,[39] [Cp*RhCl(2,2′-dipyridyl)]Cl,[40] Cp*RuCl(2,2′-dipyridyl),[41] RuCl(2-phenylpyridine-κC,N)(*p*-cymene),[42] CpIr(PPh$_3$)(CO),[43] [CpIr(PPh$_3$)(CO)I]I,[44] $[(Cp^*Ir)_2(\mu\text{-}OH)_3]OH$,[45] $[Cp^*Ir(H_2O)_3]SO_4$,[46] and colloidal IrO_2 nanoparticles (ca. 20 nm diameter)[47] were prepared according to literature procedures. Complexes of the type [Cp*Ir(N−N)Cl]Cl, with 2,2′-dipyridyl,[48] 1,10-phenanthroline,[35] and 2,2′-bipyrimidine[49,50] ligands were prepared by published procedures. NMR spectra were recorded at room temperature on 400 or 500 MHz Bruker spectrometers and referenced to the residual solvent peak (δ in ppm and J in Hz). Elemental analyses were performed by Atlantic Microlab, Inc.

[(η^5-C$_5$Me$_5$)Ir(*N*,*N*,*N*′,*N*′-Tetramethylethylenediamine)Cl]Cl. $[Cp^*IrCl_2]_2$ (0.101 g, 0.127 mmol) was dissolved in 7 mL of dichloromethane under nitrogen. To this solution was added neat *N*,*N*,*N*′,*N*′-tetramethylethylenediamine (0.05 mL, 0.3 mmol). Within minutes, the color of the solution had changed from deep orange to yellow. After stirring 2.5 h at room temperature, the reaction solution was added to 40 mL of diethyl ether and the hygroscopic yellow precipitate collected by vacuum filtration in air. Yield 0.089 g (68%). ^{1}H NMR (500 MHz, MeOD-d_4) δ 3.29 (s, 6H), 3.10−3.01 (m, 2H), 2.96 (s, 6H), 2.83−2.72 (m, 2H), 1.57 (s, 15H). ^{13}C NMR (126 MHz, MeOD-d_4) δ 89.47, 65.36, 58.55, 54.96, 9.51. Anal. Calcd for $Ir_1C_{16}H_{31}N_2Cl_2\cdot 2H_2O$. C, 34.90; H, 6.41; N, 5.09; O, 5.81. Found: C, 34.67; H, 6.34; N, 4.93; O, 6.03. Crystals suitable for X-ray diffraction study were obtained by diffusion of diethyl ether into a saturated dichloromethane solution.

[(η^5-C$_5$H$_5$)IrI$_2$]$_x$.[39,51] A 50 mL flame-dried Schlenk flask was charged with $CpIr(C_2H_4)_2$ (0.215 g, 0.686 mmol) in a nitrogen-

(34) We also find pathway D, in which a molecule of H_2O assists the proton transfer to the ppy ligand of pathway A. Nevertheless, the transition state associated with pathway D, **D-TS** (see Supporting Information), lies 14.4 kcal mol^{-1} above that of pathway C, **C-TS**.

(35) The kinetic isotope effect was computed as $k_H/k_D = \exp[(\Delta G^{\ddagger}_D - \Delta G^{\ddagger}_H)/RT]$, with $T = 298.15$ K.

(36) (a) Filippov, O. A.; Filin, A. M.; Tsupreva, V. N.; Belkova, N. V.; Lledós, A.; Ujaque, G.; Epstein, L. M.; Shubina, E. S. *Inorg. Chem.* **2006**, *45*, 3086–3096. (b) Filippov, O. A.; Tsupreva, V. N.; Golubinskaya, L. M.; Krylova, A. I.; Bregadze, V. I.; Lledós, A.; Epstein, L. M.; Shubina, E. S. *Inorg. Chem.* **2009**, *48*, 3667–3678.

(37) Lund, H.; Hammerich, O. *Organic electrochemistry*, 4th ed.; M. Dekker: New York, 2001.

(38) Ball, R. G.; Graham, W. A. G.; Heinekey, D. M.; Hoyano, J. K.; McMaster, A. D.; Mattson, B. M.; Michel, S. T. *Inorg. Chem.* **1990**, *29*, 2023–2025.

(39) Heinekey, D. M.; Millar, J. M.; Koetzle, T. F.; Payne, N. G.; Zilm, K. W. *J. Am. Chem. Soc.* **1990**, *112*, 909–919.

(40) Kolle, U.; Grutzel, M. *Angew. Chem., Int. Ed. Engl.* **1987**, *26*, 567–570.

(41) (a) Fagan, P. J.; Ward, M. D.; Calabrese, J. C. *J. Am. Chem. Soc.* **1989**, *111*, 1698–1719. (b) Koelle, U.; Kossakowski, J. *J. Organomet. Chem.* **1989**, *362*, 383–398.

(42) (a) Djukic, J.-P.; Berger, A.; Duquenne, M.; Pfeffer, M.; de Cian, A.; Kyritsakas-Gruber, N. *Organometallics* **2004**, *23*, 5757–5767. (b) Bennett, M. A.; Smith, A. K. *J. Chem. Soc., Dalton Trans.* **1974**, *2*, 233–241.

(43) Blais, M. S.; Rausch, M. D. *Organometallics* **1994**, *13*, 3557–3563.

(44) Oliver, A. J.; Graham, W. A. G. *Inorg. Chem.* **1970**, *9*, 2653–2657.

(45) Nutton, A.; Bailey, P. M.; Maitlis, P. M. *J. Chem. Soc., Dalton Trans.* **1981**, 1997–2002.

(46) Ogo, S.; Makihara, N.; Watanabe, Y. *Organometallics* **1999**, *18*, 5470–5474.

(47) Hara, M.; Waraksa, C. C.; Lean, J. T.; Lewis, B. A.; Mallouk, T. E. *J. Phys. Chem. A* **2000**, *104*, 5275–5280.

(48) Ziessel, R. *J. Chem. Soc., Chem. Commun.* **1988**, 16–17.

(49) Govindaswamy, P.; Canivet, J.; Therrien, B.; Süss-Fink, G.; Stepnicka, P.; Ludvik, J. *J. Organomet. Chem.* **2007**, *692*, 3664–3675.

(50) Gabrielsson, A.; van Leeuwen, P.; Kaim, W. *Chem. Commun.* **2006**, 4926–4927.

filled glovebox and 30 mL of dry, degassed dichloromethane was added, followed by iodine (0.185 g, 0.729 mmol). The reaction was stirred at room temperature for 1 h, during which time a fine purple-brown precipitate formed in solution. The precipitate was collected by filtration in air and washed with two 5 mL portions of dichloromethane. Yield 0.272 g (78%). As previously reported, the polymeric material is insoluble in water and most organic solvents. In DMSO-d_6, the solid dissolves to give an orange solution with a singlet in the ^{1}H NMR at 6.10 ppm. Over time, the signal at 6.10 decreases in intensity with a new singlet appearing at 6.61 ppm. Bright red crystals corresponding to the sulfur-bound DMSO adduct η^5-cyclopentadieneyl-κ^1-dimethylsulfoxo-*S*-iridium(III) iodide grew from a concentrated DMSO-d_6 solution which was allowed to stand open in air for several days (see the Supporting Information).

[(η^5-C_5H_5)IrI(2,2′-dipyridyl)]PF_6. [(η^5-C_5H_5)IrI_2]$_x$ (0.162 g, 0.317 mmol), 2,2′-dipyridyl (0.0549 g, 0.352 mmol), and potassium hexafluorophosphate (0.0881 g, 0.479 mmol) were combined in an oven-dried 50 mL Schlenk flask under nitrogen, and 30 mL of dry, degassed acetonitrile was added. The suspension was heated to 50 °C under nitrogen, gradually lightening in color until it was an entirely homogeneous solution after approximately 4 h. After being heated for 16 h, the now-yellow solution was cooled to room temperature and reduced in volume to 1−2 mL on a rotary evaporator. Addition of 50 mL of deionized water gave a yellow precipitate which was collected by filtration in air. The solid was washed first with water, then diethyl ether and finally dried in vacuo. Yield 0.158 g (73%). ^{1}H NMR (400 MHz, DMSO-d_6) δ 9.54 (d, J = 5.0 Hz, 2H), 8.80 (d, J = 8.0 Hz, 2H), 8.31 (m, 2H), 7.74 (m, 2H), 6.33 (s, 5H). ^{13}C NMR (126 MHz, DMSO-d_6) δ 157.07, 155.03, 140.49, 128.16, 124.83, 79.66. Anal. Calcd for $Ir_1I_1C_{15}H_{13}N_2P_1F_6$. C, 26.29; H, 1.91; N, 4.09. Found: C, 26.50; H, 1.79; N, 4.24.

[(η^5-C_5H_5)IrI(2,2′-dipyridyl)]NO_3. [(η^5-C_5H_5)IrI_2]$_x$ (0.1036 g, 0.203 mmol), 2,2′-dipyridyl (0.0365 g, 0.234 mmol), and tetra-*n*-butylammonium nitrate (0.0936 g, 0.307 mmol) were combined in an oven-dried 50 mL Schlenk flask under nitrogen, and 20 mL of dry, degassed acetonitrile was added. The reaction was stirred at 50 °C for 13 h before being cooled to room temperature and evaporated to dryness on a rotary evaporator. The resulting solid was dissolved in 40 mL of deionized water, and the aqueous solution was extracted with three 30 mL portions of dichloromethane. The combined organic portions were discarded, and the aqueous solution once again evaporated to dryness. The remaining solid was washed once with a 40 mL portion of a 2:1 mixture of acetone with diethyl ether to remove any residual tetra-*n*-butylammonium salts, giving 0.075 g of the product as a yellow powder (61% yield). ^{1}H NMR (500 MHz, DMSO-d_6) δ 9.54 (d, J = 5.7 Hz, 2H), 8.80 (d, J = 8.2 Hz, 2H), 8.31 (s, 2H), 7.74 (s, 2H), 6.32 (5H). ^{13}C NMR (126 MHz, DMSO-d_6) δ 157.07, 155.00, 140.47, 128.14, 124.83, 79.65. Anal. Calcd for $Ir_1I_1C_{15}H_{13}N_3O_3$. C, 29.91; H, 2.18; N, 6.98. Found: C, 29.69; H, 2.05; N, 6.89. Crystals suitable for X-ray diffraction study were obtained by diffusion of diethyl ether into a saturated acetonitrile solution.

X-ray Diffraction Studies of Compounds 6, 8, $CpIrI_2$(DMSO-S), and Cp$Ir(O\text{-}NO_2)$(bipy)PF_6. Crystal samples were mounted in a polyimide MiTeGen loop with immersion oil. All measurements were made on a Rigaku SCXMini diffractometer with filtered Mo−Kα radiation at a temperature of 223 K. Three omega scans consisting of 180 data frames each were collected with a frame width of 1.0° for compounds **6** and **8**. Two omega scans consisting of 180 data frames each were collected for $CpIrI_2$(DMSO-*S*) and Cp$Ir(O\text{-}NO_2)$(bipy)PF_6. The data frames were processed and scaled using the Rigaku CrystalClear.[52] The data were corrected for Lorentz and polarization effects. The structure was solved by direct methods and expanded using Fourier techniques.[53] The non-hydrogen atoms were refined anisotropically and hydrogen atoms were treated as idealized contributions. The final cycle of full-matrix least-squares refinement[54] on F^2 were applied until convergence of unweighted and weighted factors of $R = \sum||F_o| - |F_c||/\sum|F_o|$; $R_w = \{\sum[w(F_o^2 - F_c^2)^2]/\sum[w(F_o^2)^2]\}^{1/2}$. Crystal data and experimental details are included in the Supporting Information.

Kinetic Studies. Measurements of initial oxygen evolution rate were made with a YSI Clark-type oxygen electrode. Prior to beginning each set of experiments, the gas-permeable membrane was replaced to ensure a high-quality response. The electrode, secured in a Teflon tube, was inserted into a tight-fitting water-jacketed glass vessel. The system was kept at a constant temperature of 25 °C. In a typical experiment, a freshly prepared Ce(IV) solution in Milli-Q water (5 mL, 78 mM; pH 0.87) was allowed to equilibrate with stirring for 7 min. Data collection over 5−7 min showed equilibration of the system, and when a steady baseline was achieved, 10 μL of catalyst solution was injected. Oxygen evolution commenced immediately and typically exceeded the maximum value for the system within 10 min of injection.

For studies on oxygen evolution at longer time scales, a headspace fluorescence-probe oxygen assay was used. The apparatus (Ocean Optics, Dunedin, FL) consists of a probe (FOXY-R) and a custom glass cell with a threaded fitting for the probe and an airtight septum for purging. A fluorescent dye is embedded in a sol−gel matrix in the probe tip. Upon exposure to oxygen, the quenching of the dye's fluorescence is recorded by a fluorimeter connected to the probe via a fiber-optic cable. A Stern−Volmer plot generated from standard oxygen concentrations in the cell is then used to convert the raw fluorescence lifetime data into headspace oxygen concentration. In a typical experiment, a freshly prepared Ce(IV) solution in Milli-Q water (5 mL, 78 mM; pH 0.87) was allowed to equilibrate with stirring after being purged with nitrogen gas for 20 min. Data collection over 20 min showed equilibration of the system, and when a steady baseline had been achieved, 10 μL of catalyst solution was injected. Depending on the experimental conditions, oxygen evolution was apparent within 5 min.

Cerium(IV) ammonium nitrate (CAN) of the highest grade (99.99%) was purchased from Sigma-Aldrich and kept in a desiccator prior to use. In the case of comparative rate experiments, the pH of the solutions was adjusted by using concentrated nitric acid solutions. Deuterated cerium(IV) ammonium nitrate was prepared by dissolution of CAN in excess 99% D_2O (Cambridge Isotope Laboratories, Cambridge, MA) followed by removal of solvent under reduced pressure and drying overnight. Solutions for KIE at lower cerium(IV) loading were prepared by first acidifying solvent with HNO_3 or DNO_3 (99% DNO_3 from Cambridge Isotope Laboratories).

^{18}O Incorporation and Stable Isotope Ratio Mass Spectrometry (SIR-MS). Analyses were performed using a Thermo-Finnigan GasBench II connected to a Thermo-Finnigan Delta^{plus} XP stable isotope ratio mass spectrometer operating in continuous-flow mode. Both the GasBench and Delta^{plus} XP were controlled by Isodat software (version 3.0). Using the GasBench II, the headspace of a vial is sampled via a nested sampling needle. Helium flows (ca. 0.5 μL min^{-1}) into the vial through an upper aperture in the needle, and the resultant mixture flows back through a lower aperture and into an inner capillary. The gas mixture is then directed into a Nafion (DuPont) drying tube and out through a 10-μL sampling loop in a Valco switching valve. Once the sampling loop is flushed with headspace gas, it is switched to inject the sample in the loop onto an integral gas chromatograph with a Varian CP7551 PLOT fused silica 25 m × 0.32 mm column (coating: Poraplot Q) at 32 °C to separate O_2 from CO_2. The separated gases are then carried through a second drying tube to an open split where a glass capillary continually draws in helium and sample gases to the mass spectrometer for analysis. The dilution factor of the open split can

(51) Yamazaki, H. *Bull. Chem. Soc. Jpn.* **1971**, *44*, 582.

(52) CrystalClear and CrystalStructure, Rigaku/MSC, The Woodlands, Texas, 2005.

(53) SHELXS (direct methods): Sheldrick, G. M., 1990. SHELXL (refinement): Sheldrick, G. M.; Schneider, T. R., 1997.

be adjusted to decrease the signal intensity, if necessary. In the mass spectrometer, the samples are ionized (electron ionization) and analyzed in three cups set to O_2 peaks with masses 32, 33, and 34. The relative nominal amplifications for the three cups are 1, 100, and 300. Under the conditions we used, the sample vials are only slightly pressurized because the sampling gas mixture from the vial either was directly vented (with the Valco valve set to "inject" mode) or was vented after going through the sampling loop (with the Valco valve set to "load" mode). This technique has been described and used previously by our group.[55]

Electrochemistry. Electrochemical measurements were made on an EG&G Princeton Applied Research Model 273A potentiostat/galvanostat using a standard three-electrode configuration. A basal plane graphite electrode (surface area: 0.09 cm^2) was used as the working electrode to reduce background water oxidation. The electrode consisted of a brass cylinder, sheathed in a Teflon tube. At the tip of the brass, a two-part silver conducting epoxy (Alfa Aesar) was used to firmly attach the basal plane carbon electrode surface to the brass. Finally, the tip was sealed with the organic solvent-resistant, electrically insulating, two-part epoxy Tra-bond 2151 (Emerson and Cuming, Canton, MA). Immediately prior to experiments, the working electrode was polished with 1 μm alumina paste, washed with copious amounts of water, and allowed to dry completely. Then the surface of the working electrode was resurfaced with tape to restore the gray, basal surface.

For aqueous electrochemical experiments, a platinum wire was used as the counter electrode, and a saturated calomel electrode (SCE) was used as the reference electrode (NHE vs SCE: +241 mV). Experiments were carried out in unbuffered solutions containing 0.1 M KNO_3 (Johnson Matthey, electronics grade) as the supporting electrolyte.

For nonaqueous electrochemical studies, a platinum wire was used as the counter electrode, and Ag/0.1 M $AgNO_3$ was used as the reference electrode. Ferrocene was used as an external standard to calibrate the reference electrode versus NHE (Fc/Fc^+: +0.690 V vs NHE in MeCN).[56] Experiments were carried out in still-dried acetonitrile solution containing 0.1 M tetrabutylammonium perchlorate (Fluka, electrochemical grade) as the supporting electrolyte.

Computational Details. Calculations were performed at the DFT(B3LYP) level[57] with Gaussian03.[58] Geometry optimizations were carried out with the 6-31G** basis set for O, N, C, and H[59] and the Stuttgart−Bonn scalar relativistic ECP with associated basis set for Ir.[60] These basis sets were used to compute the energies given in the text. All geometries were fully optimized without any symmetry or geometry constrains. The nature of all stationary points was confirmed by the analytical calculation of their frequencies. The vibrational data were used to relax the geometry of each transition state toward reactants and products, in order to confirm its nature. Free energies were calculated within the harmonic approximation for vibrational frequencies. The full set of frequencies was used to calculate KIE. The effect of the solvent, water, was modeled by single-point calculations with the CPCM method.[61] The influence of the counteranion was not implemented since the cations and the anions should form separated ion pairs in water. The zero-point, thermal, entropy, and solvent corrections did not alter the energy profiles to any great extent. These corrections are given in the Supporting Information. The spin densities were obtained from NPA (Natural Population Analysis) calculations.[62]

Acknowledgment. This material is based upon work supported as part of the Argonne-Northwestern Solar Energy Research (ANSER) Center, an Energy Frontier Research Center funded by the U.S. Department of Energy, Office of Science, Office of Basic Energy Sciences under Award Number DE-PS02-08ER15944 (G.W.B., R.H.C., and J.D.B.). O.E. thanks the Ministère de l'Enseignement Supérieur et de la Recherche and the CNRS for funding. D.B. thanks Sanofi-Aventis for a postdoctoral fellowship (2007−2009) and the Spanish MICINN for his current Juan de la Cierva position. J.D.B. thanks Katherine Shinopoulos for helpful discussions.

Supporting Information Available: NMR spectra for new compounds **6**, **7**, and **8**. Time-dependent NMR spectra for $[(\eta^5\text{-}C_5H_5)IrI_2]_x$. Crystal structures and parameters for **6**, **7** ($(\eta^5\text{-}C_5H_5)IrI_2$(dimethyl sulfoxide-S), and $(\eta^5\text{-}C_5H_5)Ir(O\text{-}NO_2)$(bipy)$PF_6$. Kinetic data, log−log plots, oxygen-evolution traces, and ESI+ MS data. Cyclic voltammograms of **1**, **3**, and **6**. Optimized geometries of all stationary points reported in the article, with the associated potential and CPCM energies and the zero-point, thermal, and entropy energy corrections. Complete list of authors for ref 58. This material is available free of charge via the Internet at http://pubs.acs.org.

JA104775J

(54) Least squares function minimized: $\sum w(F_o^2 - F_c^2)^2$.
(55) Chen, H.; Tagore, R.; Olack, G.; Vrettos, J. S.; Weng, T.-C.; Penner-Hahn, J.; Crabtree, R. H.; Brudvig, G. W. *Inorg. Chem.* **2007**, *46*, 34–43.
(56) Barrette, W. C., Jr.; Johnson, H. W., Jr.; Sawyer, D. T. *Anal. Chem.* **1984**, *56*, 1560.
(57) (a) Lee, C. T.; Yang, W. T.; Parr, R. G. *Phys. Rev. B* **1988**, *37*, 785–789. (b) Becke, A. D. *J. Chem. Phys.* **1993**, *98*, 5648–5652. (c) Stephens, P.; Devlin, F.; Chabalowski, C.; Frisch, M. *J. Phys. Chem.* **1994**, *98*, 11623–11627.
(58) Frisch, M. J. et al. *GAUSSIAN 03, revision D.01*; Gaussian, Inc.: Wallingford, CT, 2004.
(59) (a) Hehre, W. J.; Ditchfield, R.; Pople, J. A. *J. Phys. Chem.* **1972**, *56*, 2257–2261. (b) Ehlers, A. W.; Böhme, M.; Dapprich, S.; Gobbi, A.; Höllwarth, A.; Jonas, V.; Köhler, K. F.; Stegmann, R.; Veldkamp, A.; Frenking, G. *Chem. Phys. Lett.* **1993**, *208*, 111–114. (c) Höllwarth, A.; Böhme, H.; Dapprich, S.; Ehlers, A. W.; Gobbi, A.; Jonas, V.; Köhler, K. F.; Stegmann, R.; Veldkamp, A.; Frenking, G. *Chem. Phys. Lett.* **1993**, *203*, 237–240. (d) Hariharan, P. C.; Pople, J. A. *Theor. Chim. Acta* **1973**, *28*, 213–222.
(60) (a) Andrae, D.; Häussermann, U.; Dolg, M.; Stoll, H.; Preuss, H. *Theor. Chim. Acta* **1990**, *77*, 123–141. (b) Bergner, A.; Dolg, M.; Küchle, W.; Stoll, H.; Preuss, H. *Mol. Phys.* **1993**, *30*, 1431–1441.
(61) Barone, V.; Cossi, M. *J. Phys. Chem. A* **1998**, *102*, 1995–2001.
(62) Reed, A. E.; Curtiss, L. A.; Weinhold, F. *Chem. Rev.* **1988**, *88*, 899–926.